Available online at www.sciencedirect.com
ScienceDirect
Trans. Nonferrous Met. Soc. China 33(2023) 1768−1778
Transactions of Nonferrous Metals Society of China
www.tnmsc.cn

Numerical analysis of arc and molten pool behaviors in high speed tandem TIG welding of titanium tubes

Dong-sheng WU[1], Jiu-ling HUANG[1], Liang KONG[1], Xue-ming HUA[1], Min WANG[1], Hua LI[2], Shou-tian LIU[2]

1. Shanghai Key Laboratory of Material Laser Processing and Modification, Shanghai Jiao Tong University, Shanghai 200240, China;
2. Zhangjiagang Huayu Nonferrous Metal Material Co., Ltd., Shanghai 215627, China

Received 23 December 2021; accepted 14 April 2022

Abstract: A high speed tandem TIG welding process was adopted to manufacture titanium welded tubes. A coupled electrode, arc and weld pool numerical model was also developed to investigate the temperature distribution, arc plasma and molten metal flows, and energy propagation of this welding process. Under the driving of the electromagnetic force, arc plasmas under the leading and trailing electrodes flowed towards each other. The Marangoni stress was much higher than the arc shear stress, and was the main driving force for the backward molten metal flow on the top weld pool surface. The calculated arc efficiency of this welding process was 79.8%. The high speed tandem TIG welding process can improve the manufacturing efficiency and quality of titanium welded tubes.

Key words: tandem TIG welding process; titanium welded tube; numerical simulation; arc plasma; molten pool

1 Introduction

Pure titanium and titanium alloy tubes possess the advantages of high specific strength at room and high temperatures, high corrosion resistance and high temperature creep resistance [1,2], thus are widely utilized in the electric power, marine engineering and petrochemical industries [3,4]. Compared with titanium seamless tubes, titanium welded tubes have similar or same chemical compositions, mechanical properties and process performances, while the production cost is much lower. Usually, a tungsten inert gas (TIG) welding process is adopted to manufacture titanium welded tubes, while the welding efficiency cannot be further improved owing to the formation of weld defects, such as humping and melt-through, in high current and high speed cases [5,6].

In order to improve the welding efficiency and quality, a high speed tandem TIG welding process was developed to successfully weld titanium plates in our previous study [7], in which a leading arc with a higher current aimed to obtain a deep penetration, and a trailing arc with a lower current heated the trailing part of the weld pool and suppressed the strong backward molten metal flow [8]. This welding process is adopted to manufacture titanium welded tubes in this study.

Energy propagation in a non-consumable gas shielded arc welding process plays an important role in the lifetime of a tungsten electrode [9] and final weld bead formation [10]. The main energy propagation mechanisms on the cathode surface are thermionic cooling, thermally conducted energy from the arc column, ion heating and radiation cooling. The main energy propagation mechanisms on the anode surface are electron condensation

Corresponding author: Liang KONG, Tel: +86-21-34202679, E-mail: ingerkongliang@sjtu.edu.cn
DOI: 10.1016/S1003-6326(23)66220-X

heating, thermally conducted energy from the arc column and radiation cooling [11]. Previous studies showed that the maximum arc temperature [12,13] and arc pressure [14,15] in a twin TIG arc were lower in comparison with a single TIG arc with a same total current; therefore, the thermally conducted energy from a twin TIG arc to the cathode and anode decreased. As the size of a twin/tandem TIG arc increased, the radiation cooling of the arc column also became strong. QIN et al [8] and JIANG et al [16] proposed that an obvious "pull−push" flow pattern defined as backward and forward molten metal flows on the top weld pool surface between two arcs existed in a high speed tandem TIG welding process. This "pull−push" flow pattern might cause more sufficient energy convection, such that the weld cooling rate in a high speed tandem TIG welding process was much higher than that in a TIG welding process.

During an arc welding process, the shape of the workpiece affects the arc behaviors as well as energy propagation. OGINO et al [17,18] investigated the arc behaviors and heat input distribution of a TIG arc with a groove surface based on a 3D numerical model, and found that the maximum heat input was located on side surfaces of the groove, and the energy efficiency was increased. DONG et al [19] proposed that in a narrow gap TIG welding process, as the shape of the workpiece surface changed from concave to convex, the arc root shrank, and the energy efficiency decreased. During the high speed tandem TIG welding process of titanium tubes, the coupling effects of leading and trailing arcs, and energy propagation become complicated owing to the high speed and upward convex anode surface, while they have not been investigated before.

In this study, a coupled electrode, arc and weld pool numerical model was built to investigate the temperature distribution, arc plasma and molten metal flows, and energy propagation in high speed tandem TIG welding of titanium tubes. Energy balance of the whole welding system was analyzed. The microstructure and mechanical properties of the joint were also studied, showing that the high speed tandem TIG welding can improve the manufacturing efficiency and quality of titanium welded tubes.

2 Numerical model and numerical simulation

2.1 Computational domain and mesh size

Figure 1 shows a three-dimensional symmetrical computational domain for the tandem TIG welding process, which includes two tungsten electrode regions, two nozzle regions, an Ar region and a titanium tube region. The leading and trailing electrode diameters, electrode spacing, and distance between electrode and base metal are 3.2, 2.4, 10 and 3 mm, respectively. In the simulation, the electrodes and nozzles are stationary. The metal flows into the computational domain through the "velocity inlet" with a velocity of 5 m/min, and flows out of the computational domain through the "pressure outlet". The maximum top surface deformation under the leading arc is measured, and the value is 0.55 mm. The bottom reinforcement is 0.16 mm. A simplified weld bead is predefined in the domain. The titanium tube motion is also considered in our numerical model. A non-uniform mesh system containing a fine mesh region and a coarse mesh region is used: 0.15 mm in the electrode tips and the titanium tube, 0.2 mm in the electrode cylinders, 0.25 mm in the Ar region and 0.3 mm in the nozzles in the fine mesh region, and 0.3 mm in the titanium tube in the coarse mesh region.

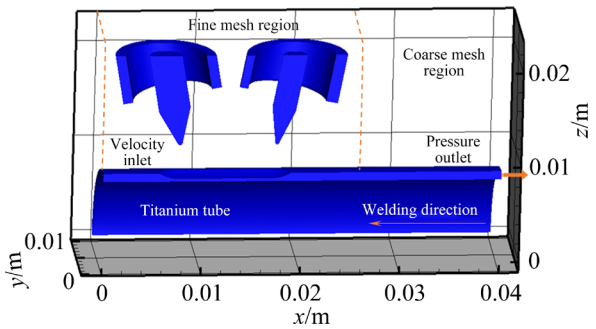

Fig. 1 Computational domain in numerical model

2.2 Governing equations

Many general assumptions are employed to simplify the numerical model for the high speed tandem TIG welding process, such as the local thermodynamic equilibrium (LTE) arc plasma [20] and Newtonian fluid. The buoyant force in the weld pool is calculated by the Boussinesq approximation,

and the metal vapour effect is neglected [21]. Governing equations for the arc and weld pool modeling include the mass, momentum, energy and current conservation equations [22].

Mass conservation equation:

$$\frac{\partial \rho}{\partial t}+\nabla\cdot(\rho \boldsymbol{v})=0 \tag{1}$$

where ρ is the fluid density, t is the time, and $\boldsymbol{v}$ is a velocity vector.

Momentum conservation equation:

$$\frac{\partial(\rho \boldsymbol{v})}{\partial t}+\nabla\cdot(\rho \boldsymbol{v}\boldsymbol{v})=-\nabla \boldsymbol{P}+\nabla\cdot\boldsymbol{\tau}+\boldsymbol{J}\times\boldsymbol{B}+\rho \boldsymbol{g} \tag{2}$$

where $\boldsymbol{P}$ is the pressure, $\boldsymbol{\tau}$ is a viscosity stress tensor, $\boldsymbol{J}$ is a current density vector, $\boldsymbol{B}$ is a magnetic flux density vector, and $\boldsymbol{g}$ is the gravitational acceleration.

Energy conservation equation:

$$\frac{\partial(\rho h)}{\partial t}+\nabla\cdot(\rho \boldsymbol{v}h)=\nabla\cdot(K\nabla T)+\boldsymbol{J}\cdot\boldsymbol{E}-S_h \tag{3}$$

where h is the enthalpy, K is the thermal conductivity, T is the temperature, $\boldsymbol{E}$ is an electric field vector, and S_h is the radiative energy loss in the arc region or the latent heat of fusion in the weld pool. The current flows from the base metal to both the leading and rearing electrodes. As the leading and trailing arcs are coupled, one current conservation equation is considered as

$$\nabla\cdot(\sigma\nabla\varphi)=0 \tag{4}$$

where σ is the electric conductivity, and φ is the electrical potential.

Ohm's law:

$$\boldsymbol{J}=-\sigma(\nabla\varphi) \tag{5}$$

Vector potential:

$$\nabla^2\boldsymbol{A}=-\mu_0\boldsymbol{J} \tag{6}$$

where $\boldsymbol{A}$ is the magnetic vector potential, and μ_0 is the magnetic permeability.

Magnetic field:

$$\boldsymbol{B}=\nabla\times\boldsymbol{A} \tag{7}$$

The electromagnetic force is calculated by $\boldsymbol{J}\times\boldsymbol{B}$.

2.3 Boundary conditions

The thermionic cooling, thermally conducted energy from the arc column, ion heating and radiation cooling on the cathode surfaces are considered in the energy boundary condition (Table 1) [23].

Table 1 External boundary conditions in numerical simulation

Boundary	v	T/K	φ	A
Top leading electrode surface (Wall)	−	300	$-\sigma\frac{\partial\varphi}{\partial n}=J_1=\frac{I_1}{\pi r_1^2}$	$\frac{\partial A}{\partial n}=0$
Top trailing electrode surface (Wall)	−	300	$-\sigma\frac{\partial\varphi}{\partial n}=J_2=\frac{I_2}{\pi r_2^2}$	$\frac{\partial A}{\partial n}=0$
Top nozzle surface (Wall)	−	300	$\frac{\partial\varphi}{\partial n}=0$	$\frac{\partial A}{\partial n}=0$
Shielding gas inlet (Mass flow inlet)	10 L/min	300	$\frac{\partial\varphi}{\partial n}=0$	$\frac{\partial A}{\partial n}=0$
Left titanium tube surface (Velocity inlet)	5.0 m/min	300	$\frac{\partial\varphi}{\partial n}=0$	$\frac{\partial A}{\partial n}=0$
Right titanium tube Surface (Pressure outlet)	−	−	$\frac{\partial\varphi}{\partial n}=0$	$\frac{\partial A}{\partial n}=0$
Bottom titanium tube surface (Wall)	−	$-h_{\mathrm{con}}\nabla T-\varepsilon_{\mathrm{r}}\alpha T^4$	0	0
Arc out surfaces (Pressure outlet)	−	300	$\frac{\partial\varphi}{\partial n}=0$	$\frac{\partial A}{\partial n}=0$

I_1 and I_2 are the leading and trailing electrode currents, respectively, r_1 and r_2 are the leading and trailing electrode radii, respectively; J_1 and J_2 are current densities on the top leading and trailing electrode surfaces, respectively

On the leading electrode surface:

$$H_{\mathrm{l}}=-\left|J_{\mathrm{el}}\right|\varphi_{\mathrm{c}}+\left|J_{\mathrm{il}}\right|V_{\mathrm{i}}+K\frac{\partial T}{\partial n}-\varepsilon_{\mathrm{r}}\alpha T^{4} \tag{8}$$

On trailing electrode surface:

$$H_{\mathrm{r}}=-\left|J_{\mathrm{er}}\right|\varphi_{\mathrm{c}}+\left|J_{\mathrm{ir}}\right|V_{\mathrm{i}}+K\frac{\partial T}{\partial n}-\varepsilon_{\mathrm{r}}\alpha T^{4} \tag{9}$$

where H_{l} and H_{r} are the energy fluxes on the leading and trailing electrode surfaces, respectively, J_{el} and J_{er} are the electron current densities on the leading and trailing electrode surfaces, respectively, J_{il} and J_{ir} are the ion current densities at the leading and trailing electrode surfaces, respectively, φ_{c} is the work function of the cathode, V_{i} is the ionization potential of Ar, n is the displacement in the direction normal to the surface, ε_{r} is the surface radiation emissivity, and α is the Stefan-Boltzmann constant.

The electron condensation heating, thermally conducted energy from the arc column, and radiation cooling on the top anode surface are considered in the energy boundary condition [24].

$$H_{\mathrm{a}}=\left|J\right|\varphi_{\mathrm{a}}+K\frac{\partial T}{\partial n}-\varepsilon_{\mathrm{r}}\alpha T^{4} \tag{10}$$

where H_{a} is the energy flux on the top anode surface, and φ_{a} is the work function of the anode.

The bottom titanium tube surface cannot get any energy from the arc column, so only convective energy transfer and radiation cooling are considered in the energy boundary condition.

$$H_{\mathrm{b}}=-h_{\mathrm{con}}\left(T-T_{0}\right)-\varepsilon_{\mathrm{r}}\alpha T^{4} \tag{11}$$

where H_{b} is the energy flux on the bottom tube surface, h_{con} is the convective heat transfer coefficient, and T_0 is the ambient temperature.

The Marangoni stress and arc shear stress are considered in the tangential momentum boundary condition of the top weld pool surface [25]:

$$-\mu\frac{\partial \boldsymbol{v}_{\mathrm{t}}}{\partial n}=\frac{\partial \boldsymbol{\gamma}}{\partial T}\frac{\partial T}{\partial \boldsymbol{S}}-\mu_{\mathrm{p}}\frac{\partial \boldsymbol{v}_{\mathrm{p}}}{\partial n} \tag{12}$$

where $\boldsymbol{\gamma}$ is the surface tension.

Only the Marangoni stress is considered in the tangential momentum boundary condition of the bottom weld pool surface:

$$-\mu\frac{\partial \boldsymbol{v}_{\mathrm{t}}}{\partial n}=\frac{\partial \boldsymbol{\gamma}}{\partial T}\frac{\partial T}{\partial \boldsymbol{S}} \tag{13}$$

where μ is the fluid viscosity, $\boldsymbol{v}_{\mathrm{t}}$ is the tangential fluid velocity, $\boldsymbol{S}$ is the tangential vector, μ_{p} is the arc plasma viscosity, and $\boldsymbol{v}_{\mathrm{p}}$ is the arc plasma velocity.

2.4 Numerical simulation

The computational fluid dynamics (CFD) software ANSYS FLUENT was used to solve the governing equations and boundary conditions. The current conservation equation and magnetic vector equation were treated using the User-Defined Scalar (UDS) equations. The pressure and velocity coupling were dealt with following the pressure-implicit with splitting of operators (PISO) numerical procedure. The mass, momentum and energy conservation equations, and UDS equations all adapt the second order upwind discretization scheme. The convergence criterion for the residual of energy is 1×10^{-6}, and the rests are 1×10^{-3}.

3 Welding procedures

During the welding, a tandem TIG welding power source (MPT−500D) was used. The W-ThO_2 electrodes were adopted. The TA2 titanium strips with a thickness of 0.7 mm were exported through a skewed roller, and were processed into tubes through various types of roll molds. The tubes were fed at a speed of 5 m/min, and welded by the high speed tandem TIG welding. The density, thermal conductivity, electrical conductivity, specific heat and viscosity of TA2 are shown in Fig. 2. Other thermo-physical material properties of TA2 can be seen in Table 2. After forming, the tube radius was about 9.55 mm. The leading and trailing TIG torches were fixed, while the titanium tube moved. The welding wire was not used in the experiment.

The welding parameters are listed in Table 3. A sample photo of the titanium welded tube is shown in Fig. 3. The bead was cut and mounted, and then polished and finally etched using a 5 mL HF + 10 mL HNO_3 + 85 mL H_2O solution for 30 s; the weld microstructure was observed using an optical microscope. The tensile test, flattening test and flaring test were carried out according to the GB/T3625—2007 standard.

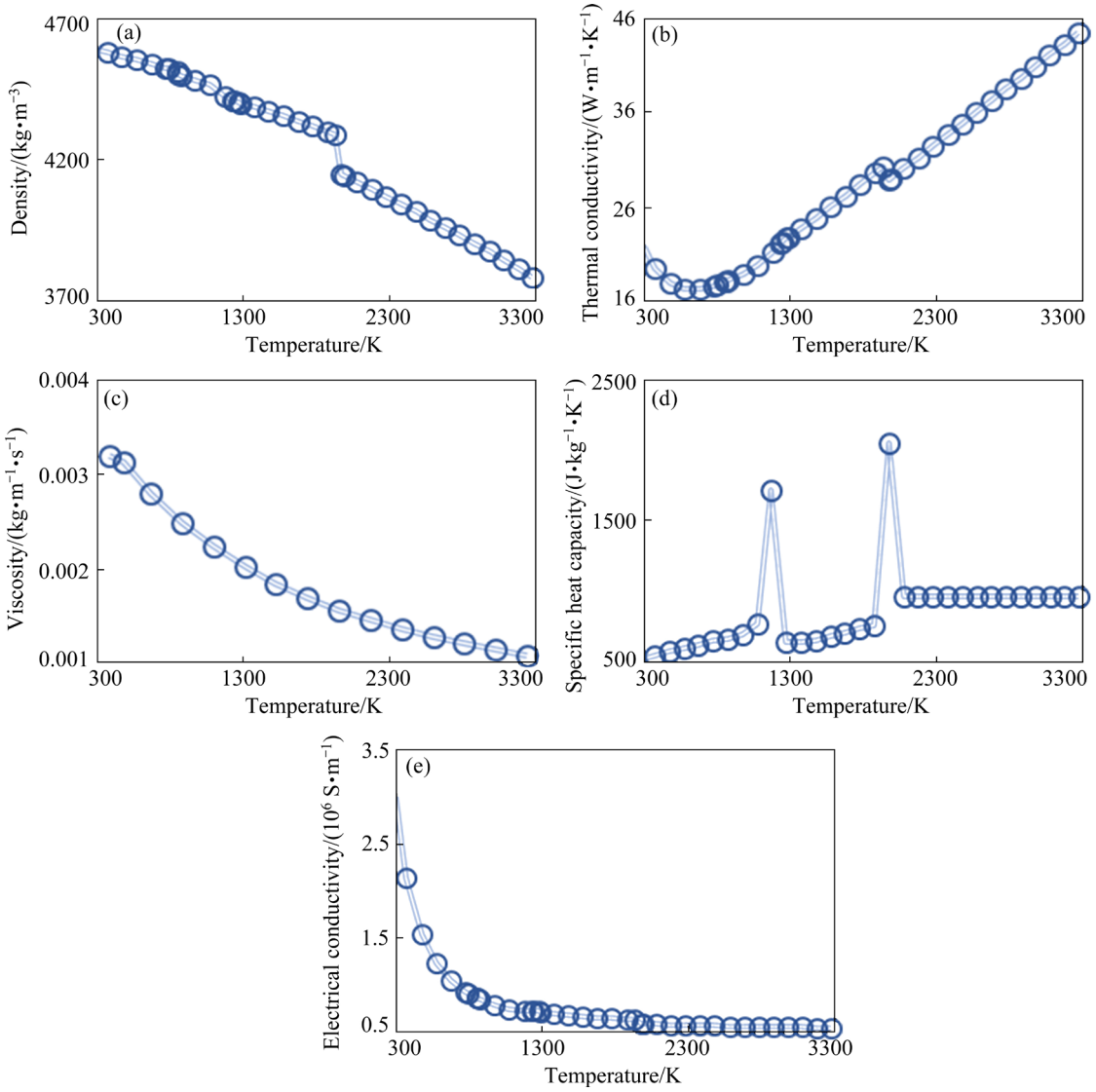

Fig. 2 Thermo-physical material properties of pure titanium (TA2): (a) Density; (b) Thermal conductivity; (c) Viscosity; (d) Specific heat capacity; (e) Electrical conductivity

Table 2 Thermo-physical properties of pure titanium (TA2)

Melting temperature/ K	Coefficient of thermal expansion/ K^{-1}	Emissivity	Surface tension gradient/ $(N·m^{-1}·K^{-1})$
1941.2	$8.9×10^{-6}$	0.63	−0.00015

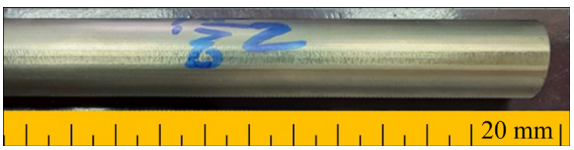

Fig. 3 Photo of titanium welded tube fabricated by high speed tandem TIG welding

Table 3 Welding parameters

Leading/ trailing electrode diameter/mm	Leading/ trailing tip angle/(°)	Electrode height/ mm	Electrode spacing/ mm
3.2/2.4	45/ 30	3.0	10
Leading/ trailing electrode angle/(°)	**Leading/ trailing welding current/A**	**Welding speed/ $(m·min^{-1})$**	**Shielding gas (Ar) flow rate/ $(L·min^{-1})$**
100/80	160/70	5.0	10

4 Results and discussion

4.1 Temperature distribution, arc plasma and molten metal flows

The temperature distribution of the electrodes,

arc and weld pool in the symmetry plane is shown in Fig. 4. In the high speed tandem TIG welding, the polarities of the leading and trailing electrodes are same, so arcs attract each other under the influence of the electromagnetic force. The maximum arc temperature (17535 K) locates in the region below the leading electrode. The maximum leading electrode temperature and weld pool temperature located in the regions near the leading arc are 3743 and 3149 K, respectively. Two high temperature regions can be seen in the weld pool.

As shown in Fig. 5, in the symmetry plane, the arc plasma under the leading electrode flows downwards with a maximum velocity of 226 m/s. After striking the top anode surface, the arc plasma flows outwards parallel to the convex surface, which is similar to the case with a flat surface [26]. As the trailing electrode current is much low, the arc plasma under the trailing electrode firstly flows downwards and towards the leading electrode, but then flows upwards.

As shown in Fig. 6, two high temperature regions form on the top weld pool surface under the leading and trailing arcs. The molten metal flows backwards behind both the leading and trailing arcs with a maximum velocity of 1.04 m/s. Previous studies proposed that a “pull−push” flow pattern was defined as a backward molten metal flow after the leading arc and a forward molten metal flow before the trailing arc existed in a high speed tandem TIG weld pool [8,16]. This flow pattern can also be observed in a tandem/twin MIG weld pool [27,28], a TIG-MIG weld pool [29] and a hybrid plasma-MIG pool [30]. However, QIN et al [8] proposed that when the trailing arc was seriously deflected to the leading arc in a high speed tandem TIG welding process, the arc pressure of the hybrid arc decreased, and the molten metal mainly flowed backwards.

As shown in Fig. 7, owing to the outward flow of the leading arc plasma, in the x direction, the arc shear stress acting on the top weld pool surface is negative before the leading arc, and positive after the leading arc. Owing to the arc attraction, the trailing arc plasma mainly flows forwards, so in the x direction, the arc shear stress acting on the top weld pool surface near the trailing arc is negative. In the y direction, the arc shear stress is mainly positive near both the leading and trailing arcs.

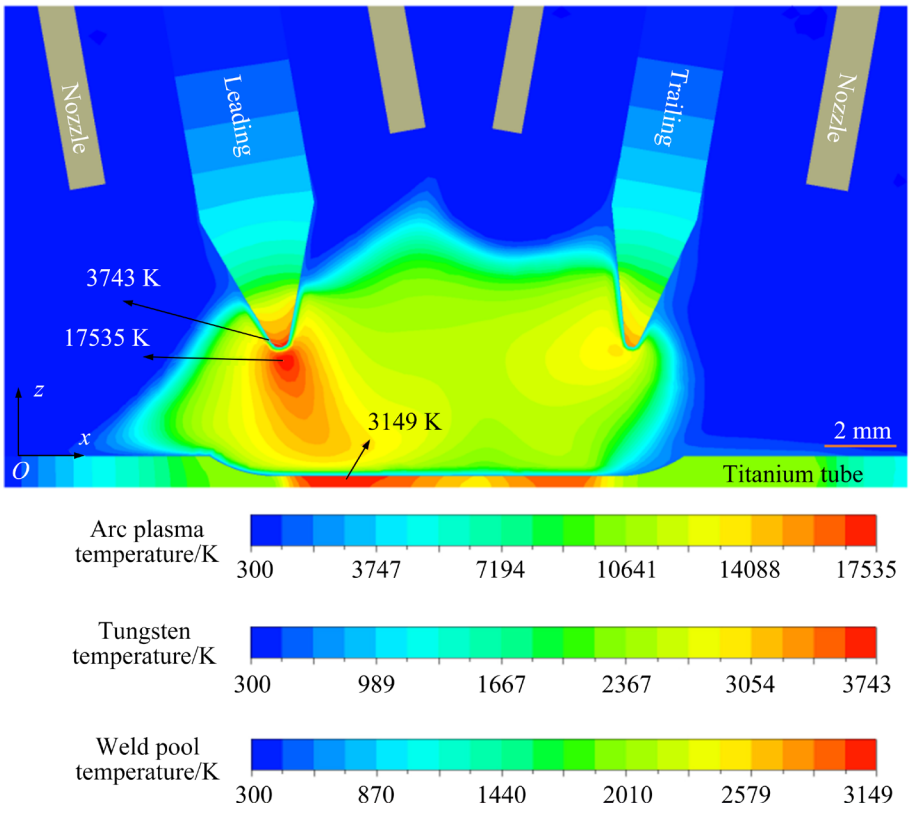

Fig. 4 Temperature distribution of electrodes, arc and weld pool in symmetry plane

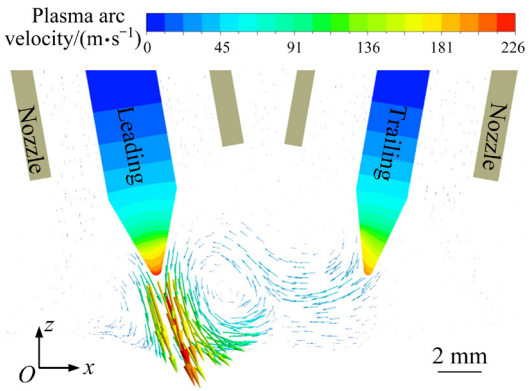

Fig. 5 Arc plasma flow in symmetry plane

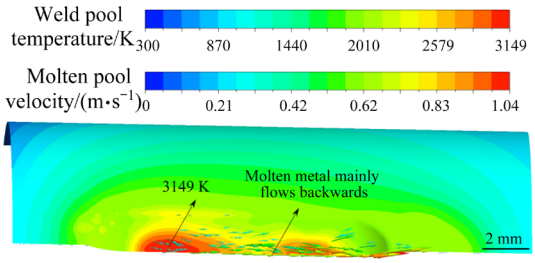

Fig. 6 Molten metal temperature and flow on top weld pool surface

In the x direction, the Marangoni stress acting on the top weld pool surface is negative before the leading arc, and mainly positive after both the leading and trailing arcs. In the y direction, the Marangoni stress acting on the top weld pool surface is mainly positive near both the leading and trailing arcs.

In this high speed tandem TIG welding process,

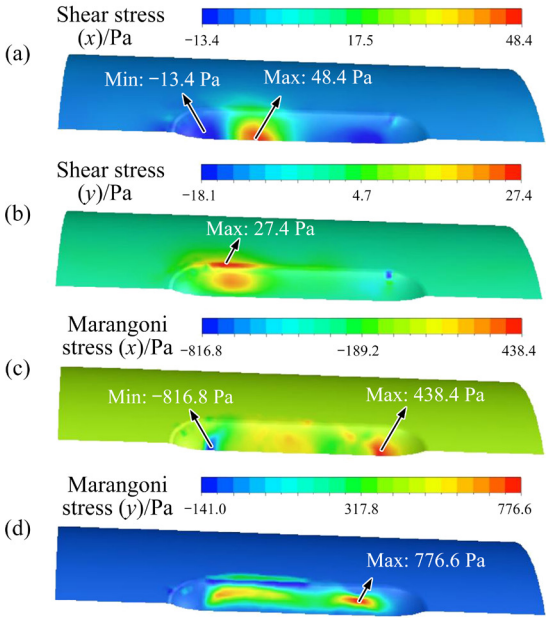

Fig. 7 Arc shear stress (a, b) and Marangoni stress (c, d) distributions: (a, c) x direction; (b, d) y direction

the trailing electrode current is much low, so the trailing arc is seriously deflected to the leading arc under the influence of the electromagnetic force. The Marangoni stress is much higher than the arc shear stress, and causes the backward molten metal flow on the top weld pool surface.

4.2 Arc energy balance and efficiency of welding system

Energy balance of the whole welding system is shown in Fig. 8. For the leading electrode, the joule heat, conduction energy from the arc and ion

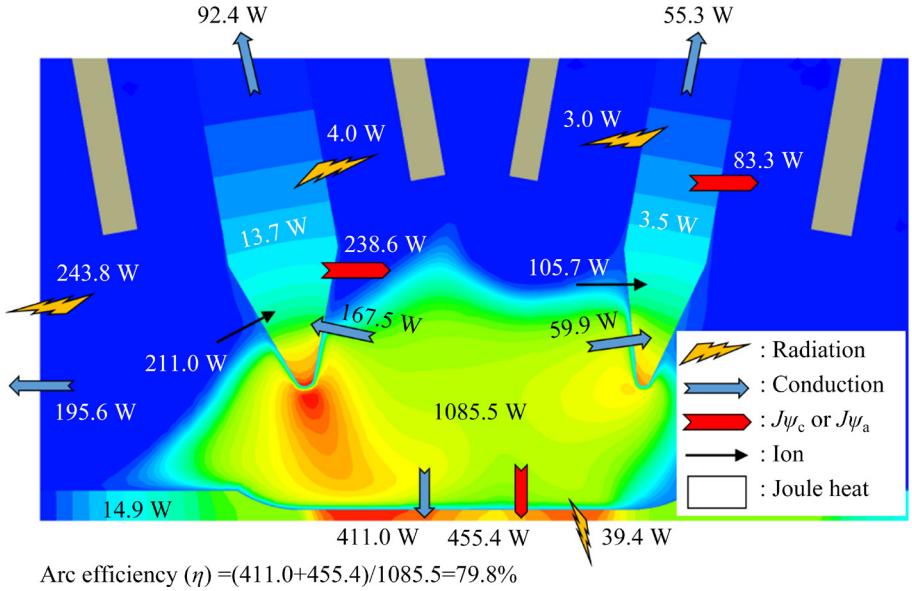

Arc efficiency (η) =(411.0+455.4)/1085.5=79.8%

Fig. 8 Energy balance and efficiency of whole welding system

heating are 13.7, 167.5 and 211.0 W, respectively; the thermionic cooling, conduction energy loss through the electrode top and radiation loss are 238.6, 92.4 and 4.0 W, respectively. For the trailing electrode, the joule heat, conduction energy from the arc and ion heating are 3.5, 59.9 and 105.7 W, respectively; the thermionic cooling, conduction energy loss through the electrode top and radiation loss are 83.3, 55.3 and 3.0 W, respectively.

For the arc, the joule heat is 1085.5 W. The conduction energy loss to the environment and radiation loss are 195.6 and 243.8 W, respectively.

For the anode, the joule heat, conduction energy from the arc and thermionic heating are 14.9, 411.0 and 455.4 W, respectively. The radiation loss is 39.4 W.

The arc energy efficiency is defined as the ratio of the total arc energy absorbed by the weld pool to the arc joule heat. The calculated arc efficiency of the high speed tandem TIG welding is about 79.8%. MURPHY et al [24] showed that the calculated TIG arc efficiency was 82%. STENBACKA [31] proposed that the average TIG arc efficiency was about 77%. Based on a calorimetric study of TIG welding of aluminum, CANTIN and FRANCIS [32] measured the TIG arc efficiency, and found that the arc efficiency in the electrode negative polarity (about 80%) was higher than that in the electrode positive polarity (about 60%). In summary, the calculated arc efficiency of a tandem TIG arc in this study is reasonable.

4.3 Weld microstructure and mechanical properties

The weld microstructure of the high speed tandem TIG welding is shown in Fig. 9. Fine equiaxed α grains exist in the base metal. Jagged grains form in the heat affected zone (HAZ) close to the base metal (Region 1 and Region 2). As shown in Region 3, coarser jagged grains form in

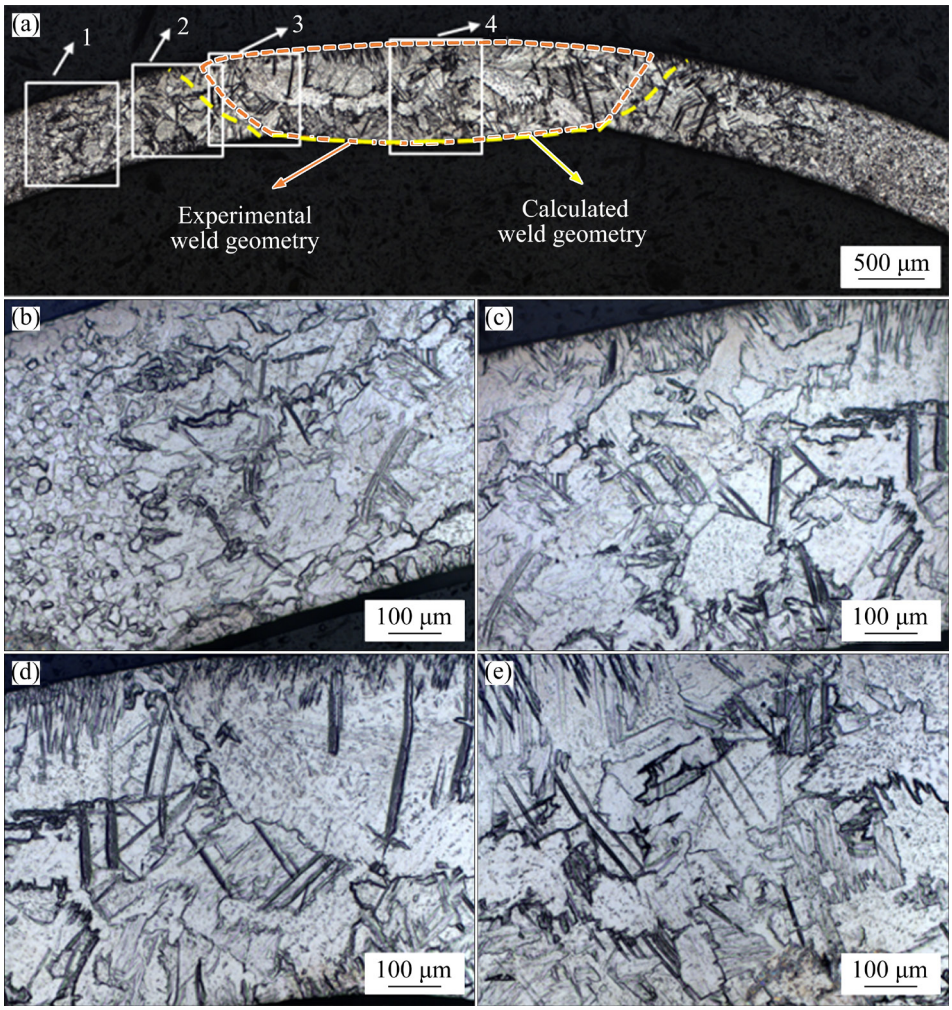

Fig. 9 Weld microstructure of high speed tandem TIG welding (a), and microstructures of Region 1 (b), Region 2 (c), Region 3 (d) and Region 4 (e)

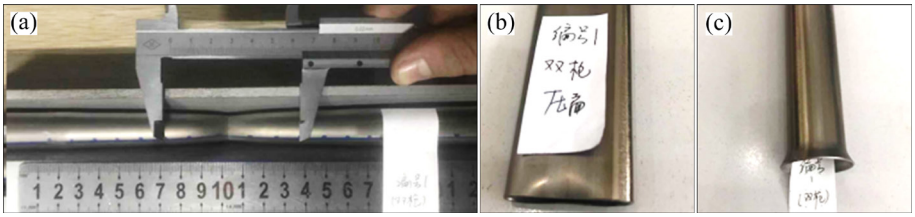

Fig. 10 Mechanical test samples of titanium welded tube: (a) Tensile test; (b) Flattening test; (c) Flaring test

the HAZ close to the fusion zone (FZ). In the FZ, there are many coarse equiaxed dendrite grains, and a few fine equiaxed dendrite grains. The calculated top and bottom weld widths are 3.85 and 2.57 mm, respectively. The experimental top and bottom weld widths are 3.39 and 2.41 mm, respectively.

Both in the numerical simulation and experiment, no weld defect forms in this welding process. As shown in Fig. 10, clear necking can be observed in the fracture location. The tensile strength, yield strength and elongation of the tube fabricated by the high speed tandem TIG welding are 458.26 MPa, 357.42 MPa and 36%, respectively. No crack forms in the weld after flattening and flaring tests. In summary, the joint made by the high speed tandem TIG welding meets the requirements of the GB/T3625—2007 standard.

5 Validation of numerical simulation

SADEK et al [33] measured the W−ThO_2 electrode temperature distribution with a current of 150 A, an electrode diameter of 2.4 mm and a tip angle of 45°, and found that the maximum electrode temperature was about 3600 K. TANAKA et al [11] calculated the temperature and velocity distributions of a TIG arc with a current of 150 A, an electrode diameter of 3.2 mm and a tip angle of 60°, and found that the maximum arc temperature was about 17000 K. HAIDAR et al [34] found that the arc current and cathode tip had great influences on the electrode and arc temperature distributions. In this study, with a leading current of 160 A, an electrode diameter of 3.2 mm and a tip angle of 45°, the calculated maximum electrode and arc temperatures are 3743 and 17535 K, respectively. As shown in Fig. 10, the calculated weld geometry also agrees well with the experiment result. In summary, the calculated arc efficiency, maximum electrode and arc temperatures, and weld geometry are acceptable.

6 Conclusions

(1) As the trailing electrode current is much low, under the influence of the electromagnetic force, the trailing arc is seriously deflected to the leading arc.

(2) The “pull−push” molten metal flow pattern proposed in previous hybrid arc welding studies is not formed in this case. The Marangoni stress on the top weld pool surface is stronger than the arc shear stress, and mainly positive after the leading and trailing arcs in the x and y directions, so the molten metal on the top weld pool surface mainly flows backwards.

(3) The calculated arc efficiency of the high speed tandem TIG welding is 79.8%.

(4) The tube fabricated by the high speed tandem TIG welding meets the requirements of the GB/T3625—2007 standard.

Acknowledgments

This research is supported by the National Key R&D Program of China (No. 2016YFB0301205).

References

[1] PENG He-li, LI Xi-feng, CHEN Xu, JIANG Jun, LUO Jing-feng , XIONG Wei, CHEN Jun. Effect of grain size on high-temperature stress relaxation behavior of fine-grained TC4 titanium alloy [J]. Transactions of Nonferrous Metals Society of China, 2020, 30(3): 668−677.

[2] XU Zheng-zheng, DONG Zhi-qiang, YU Zhao-hui, WANG Wen-ke, ZHANG Jian-xun. Relationships between microhardness, microstructure, and grain orientation in laser-welded joints with different welding speeds for Ti6Al4V titanium alloy [J]. Transactions of Nonferrous Metals Society of China, 2020, 30(5): 1277−1289.

[3] MAHAMOOD R M, AKINLABI E T. Corrosion behavior of laser additive manufactured titanium alloy [J]. The

International Journal of Advanced Manufacturing Technology, 2018, 99(5): 1545−1552.

[4] CUI Shu-wan, SHI Yong-hua, ZHANG Cheng-shi. Microstructure and mechanical properties of TC4 titanium alloy K-TIG welded joints [J]. Transactions of Nonferrous Metals Society of China, 2021, 31(2): 416−425.

[5] MENG Xiang-meng, QIN Guo-liang, ZOU Zeng-da. Investigation of humping defect in high speed gas tungsten arc welding by numerical modelling [J]. Materials & Design, 2016, 94: 69−78.

[6] ABBASI Z, YUHAS D, ZHANG Lu, BASANTES A D C, TEHRANI N N, OZEVIN D, INDACOCHEA E. The detection of burn-through weld defects using noncontact ultrasonics [J]. Materials, 2018, 11(1): 128−143.

[7] HUANG Jiu-ling, KONG Liang, WANG Min, WU Dong-sheng, LI Fang. Pure titanium TA2 thin plate double tungsten electrode argon arc welding process [J]. Transactions of the China Welding Institution, 2019, 40(9): 14−18.

[8] QIN Guo-liang, MENG Xiang-meng, FU Bang-long. High speed tandem gas tungsten arc welding process of thin stainless steel plate [J]. Journal of Materials Processing Technology, 2015, 220: 58−64.

[9] LIU Zu-ming, FANG Yue-xiao, CHEN Shi-yu, ZHANG Tao, LV Zhen-yu, LUO Zhen. Focusing cathode tip characteristics in cooling tungsten [J]. Energy, 2019, 167: 982−993.

[10] van NGUYEN A, TASHIRO S, TANAKA M. Undercut formation mechanism in keyhole plasma arc welding [J]. Welding Journal, 2019, 98: 204s−212s.

[11] TANAKA M, YAMAMOTO K, TASHIRO S, NAKATA K, YAMAMOTO E, YAMAZAKI K, SUZUKI K , MURPHY A B, LOWKE J J. Time-dependent calculations of molten pool formation and thermal plasma with metal vapour in gas tungsten arc welding [J]. Journal of Physics D: Applied Physics, 2010, 43(43): 434009.

[12] WANG Xin-xin, FAN Ding, HUANG Jian-kang, HUANG Yong. Numerical simulation of heat transfer and fluid flow in double electrodes TIG arc-weld pool [J]. Acta Metallurgica Sinca, 2015, 51(2): 178−190.

[13] NOMURA K, SHIRAI K, KISHI T, HIRATA Y. Study on temperature measurement of two-electrode TIG arc plasma [J]. Welding International, 2015, 29(7): 493−501.

[14] ZHANG Guang-jun, LENG Xue-song, WU Lin. Physics characteristic of coupling arc of twin-tungsten TIG welding [J]. Transactions of Nonferrous Metals Society of China, 2006, 16(4): 813−817.

[15] SCHWEDERSKY M B, GONÇALVES E, SILVA R H, DUTRA J C, REISGEN U, WILLMS K. Two-dimensional arc stagnation pressure measurements for the double-electrode GTAW process [J]. Science and Technology of Welding and Joining, 2016, 21(4): 275−280.

[16] JIANG Hai-yong, QIN Guo-liang, FENG Chao, MENG Xiang-meng. High-speed tandem pulsed GTAW of thin stainless steel plate [J]. Welding Journal, 2019, 98(8): 215s−226s.

[17] OGINO Y, HIRATA Y, NOMURA K. Heat input and pressure distribution of TIG arc on groove surface [J]. Welding in the World, 2011, 55(11): 107−113.

[18] OGINO Y, NOMURA K, HIRATA, Y. Numerical analysis of arc plasma behaviour in groove welding with 3D TIG arc model [J]. Welding International, 2013, 27(11): 867−873.

[19] DONG Bo-lun, CAI Xiao-yu, NI Zhi-da, LIN San-bao, FAN Cheng-lei, YANG Chun-li. Numerical simulation of arc characteristics in narrow gap TIG welding [J]. International Journal of Mechanical Sciences, 2019, 161/162: 105031.

[20] LU Shan-ping, DONG Wen-chao, LI Dian-zhong, LI Yi-yi. Numerical study and comparisons of gas tungsten arc properties between argon and nitrogen [J]. Computational Materials Science, 2009, 45(2): 327−335.

[21] SAVAŞ A, CEYHUN V. Finite element analysis of GTAW arc under different shielding gases [J]. Computational Materials Science, 2012, 51(1): 53−71.

[22] WU Dong-sheng, TASHIRO S, HUA Xue-ming, TANAKA M. Coupled mechanisms of the keyhole, energy transfer and compositional change associated with the variable polarity plasma arc process [J]. Journal of Physics D: Applied Physics, 2021, 54(11): 115204.

[23] LIU Zheng-jun, LI Yu-hang, SU Yun-hai. Simulation and analysis of heat transfer and fluid flow characteristics of arc plasma in longitudinal magnetic field-tungsten inert gas hybrid welding [J]. The International Journal of Advanced Manufacturing Technology, 2018, 98(5): 2015−2030.

[24] MURPHY A B, TANAKA M, YAMAMOTO K, TASHIRO S, LOWKE J J, OSTRIKOV K. Modelling of arc welding: The importance of including the arc plasma in the computational domain [J]. Vacuum, 2010, 85(5): 579−584.

[25] TANAKA M, USHIO M, LOWKE J J. Numerical study of gas tungsten arc plasma with anode melting [J]. Vacuum, 2004, 73(3/4): 381−389.

[26] LAGO F, GONZALEZ J J, FRETON P, GLEIZES A. A numerical modelling of an electric arc and its interaction with the anode: Part I. The two-dimensional model [J]. Journal of Physics D: Applied Physics, 2004, 37(6): 883−897.

[27] UEYAMA T, OHNAWA T, TANAKA M, NAKATA K. Effects of torch configuration and welding current on weld bead formation in high speed tandem pulsed gas metal arc welding of steel sheets [J]. Science and Technology of Welding and Joining, 2005, 10(6): 750−759.

[28] WU Dong-sheng, HUA Xue-ming, YE Ding-jian, LI Fang. Understanding of humping formation and suppression mechanisms using the numerical simulation [J]. International Journal of Heat and Mass Transfer, 2017, 104: 634−643.

[29] ZONG Ran, CHEN Ji, WU Chuan-song. A comparison of TIG-MIG hybrid welding with conventional MIG welding in the behaviors of arc, droplet and weld pool [J]. Journal of Materials Processing Technology, 2019, 270: 345−355.

[30] WU Dong-sheng, TASHIRO S, WU Zi-ang, NOMURA K, HUA Xue-ming, TANAKA M. Analysis of heat transfer and material flow in hybrid KPAW-GMAW process based on the novel three dimensional CFD simulation [J]. International Journal of Heat and Mass Transfer, 2020, 147: 118921.

[31] STENBACKA N. On arc efficiency in gas tungsten arc welding [J]. Soldagem & Inspeção, 2013, 18(4): 380−390.
[32] CANTIN G M D, FRANCIS J A. Arc power and efficiency in gas tungsten arc welding of aluminium [J]. Science and Technology of Welding and Joining, 2005, 10(2): 200−210.
[33] SADEK A A, USHIO M, MATSUDA F. Effect of rare earth metal oxide additions to tungsten electrodes [J]. Metallurgical Transactions A, 1990, 21(12): 3221−3236.
[34] HAIDAR J, FARMER A J D. Surface temperature measurements for tungsten-based cathodes of high-current free-burning arcs [J]. Journal of Physics D: Applied Physics, 1995, 28(10): 2089−2094.

钛管高速双枪 TIG 焊电弧和熔池动态行为的数值模拟

吴东升[1]，黄九龄[1]，孔 谅[1]，华学明[1]，王 敏[1]，李 华[2]，刘守田[2]

1. 上海交通大学 上海市激光制造与材料改性重点实验室，上海 200240；
2. 张家港华裕有色金属材料有限公司，上海 215627

摘 要：采用高速双枪 TIG 焊制造钛焊管。建立双钨极、双电弧和熔池耦合数学模型，研究温度场分布、电弧等离子体和熔池液态金属流动以及双枪 TIG 焊系统能量传输行为。电弧极性相同，在电磁力作用下，前后电极下方的电弧等离子体相向流动。熔池 Marangoni 力远高于电弧剪切力，是熔池上表面液态金属后向流动的主要驱动力。计算的双钨极电弧热效率为 79.8%。高速双枪 TIG 焊可以提高钛焊管的制造效率和质量。

关键词：双枪 TIG 焊；钛焊管；数值模拟；电弧等离子体；熔池

(Edited by Xiang-qun LI)